The current issue and full text archive of this journal is available at
www.emeraldinsight.com/0961-5539.htm

Multi-resolution simulation of double-diffusive convection in porous media

Received 28 August 2008
Revised 21 December 2008,
2 February 2009
Accepted 12 February 2009

J.W. Peterson
Texas Advanced Computing Center, The University of Texas at Austin, Austin, Texas, USA
B.T. Murray
Department of Mechanical Engineering, SUNY Binghamton, Vestal, New York, USA, and
G.F. Carey
Institute for Computational Engineering and Sciences, The University of Texas at Austin, Austin, Texas, USA

Abstract

Purpose – The purpose of this paper is to consider double-diffusive convection in a heated porous medium saturated with a fluid. Of particular interest is the case where the fluid has a stabilizing concentration gradient and small diffusivity.

Design/methodology/approach – A fully-coupled stabilized finite element scheme and adaptive mesh refinement (AMR) methodology are introduced to solve the resulting coupled multiphysics application and resolve fine scale solution features. The code is written on top of the open source finite element library `LibMesh`, and is suitable for parallel, high-performance simulations of large-scale problems.

Findings – The stabilized adaptive finite element scheme is used to compute steady and unsteady onset of convection in a generalized Horton-Rogers-Lapwood problem in both two and three-dimensional domains. A detailed study confirming the applicability of AMR in obtaining the predicted dependence of solutal Nusselt number on Lewis number is given. A semi-permeable barrier version of the generalized HRL problem is also studied and is believed to present an interesting benchmark for AMR codes owing to the different boundary and internal layers present in the problem. Finally, some representative adaptive results in a complex 3D heated-pipe geometry are presented.

Originality/value – This work demonstrates the feasibility of stabilized, adaptive finite element schemes for computing simple double-diffusive flow models, and it represents an easily-generalizable starting point for more complex calculations since it is based on a highly-general finite element library. The complementary nature of h-adaptivity and stabilized finite element techniques for this class of problem is demonstrated using particularly simple error indicators and stabilization parameters. Finally, an interesting double-diffusive convection benchmark problem having a semi-permeable barrier is suggested.

Keywords Convection, Porous materials, Simulation, Pipes, Meshes

Paper type Research paper

1. Introduction

Double-diffusive convection in a porous medium, like its counterpart in a viscous fluid, exhibits a wide range of interesting convective flow structure and behavior.

One author (BTM) was supported by a Visiting Faculty Fellowship from the Institute for Computational Engineering and Sciences at the University of Texas at Austin. The authors are deeply indebted to the other members of the CFDLab `LibMesh` development team, and especially to lead developers Benjamin Kirk and Roy Stogner, for their valuable insights on the development of the simulation software. Additional support was provided by NASA Grant NGT5-139, and the computations were performed on systems provided by the Texas Advanced Computing Center (TACC).

International Journal of Numerical Methods for Heat & Fluid Flow
Vol. 20 No. 1, 2010
pp. 37-65

0961-5539
DOI 10.1108/09615531011008118

Double-diffusive effects occur when there are opposing gradients of two diffusing components (commonly heat and a solute) that each affect the density of the fluid. The coupled interaction of the two diffusing components can have a significant impact on the stability of fluid-saturated porous media in a variety of relevant problem geometries. Perhaps more significant is the role played by double-diffusive convection in effecting the transport of heat and species for a wide range of steady-state or transient flow configurations. The flow structure and transport behavior associated with double-diffusive convection has applications in a broad range of areas including geophysics, energy engineering, biophysics and materials processing. Some specific examples where double-diffusive convection in a saturated porous medium is important include: geothermal natural convection (Cheng, 1978; Jellinek *et al.*, 1999; Jellinek and Kerr, 1999), contaminant transport in aquifers and ocean sediment (Hickox *et al.*, 1982; Gartling, 1982) gravitactic microorganism motion (Nguyen-Quang *et al.,* 2008) and solute segregation in the mushy zone of solidifying alloys (Heinrich and Poirer, 2004; Felicelli *et al.*, 1998; Zabaras and Samanta, 2004).

There is an extensive literature on double-diffusive convection encompassing many disciplines and spanning more than 40 years. The reference works (Nield and Bejan, 1999; Diersch and Kolditz, 2002; Rudraiah *et al.*, 2003; Lewis *et al.,* 2004; Gobin and Goyeau, 2008; Heinrich and Pepper, 1999) contain extensive bibliographies pertaining to the broad-ranging aspects of double-diffusive convection in porous media. Much of the early work on the topic was approached from the viewpoint of hydrodynamic stability, and considered the classical configuration of a horizontal layer of fluid-saturated porous medium subject to vertical temperature and solute concentration gradients.

The linear stability of this problem was analyzed by Nield (1968). If the layer is heated from below (with gravity oriented downwards) and saturated with a fluid having a stabilizing solute concentration gradient, then stability theory predicts the onset of convection from the basic motionless state to be oscillatory. This is referred to as the “diffusive” regime; the component with the larger diffusivity (heat) is destabilizing, while the slower diffusing component (solute) is stabilizing. It is well understood that this oscillatory state is subcritical, and steady convection eventually predominates. A thorough study of the bifurcation behavior for this case is presented in (Mamou and Vasseur (1999). The opposite case (solute destabilizing) is referred to as the “fingering regime” (Luo *et al.,* 2008).

For double-diffusive effects resulting from temperature and solute concentration gradients (thermosolutal convection), the large difference in the diffusivities of the two species (typically a factor of 100 or more) has a significant impact on the flow structure and heat and mass transfer. The small diffusivity associated with solute transfer leads to sharp gradients near boundaries and within the domain. Hence, reliable, accurate and efficient computations for double-diffusive convection remain an area of active research (Sezai, 2002; Zhan and Li, 2003; Bennacer *et al.*, 2003; Rebaï *et al.*, 2008) and adaptive mesh refinemat (AMR) strategies remain relatively unexplored for this problem class.

The present study considers the nonlinear multiphysics, multiscale behavior of buoyancy-driven, double-diffusive convection in a porous medium. The flow is assumed to be incompressible and the Boussinesq approximation is employed. The governing equations (section 2) are Darcy’s flow law, the pseudo-fluid model energy equation, and the equation for solute conservation. The open-source, C++ finite element library, `LibMesh` (Kirk, 2006) is used to implement an adaptive mesh refinement solution strategy in conjunction with the SUPG scheme as described in section 3. Of particular interest are the AMR strategy and the impact of stabilization when the effective solute diffusivity is much less than the thermal diffusivity.

2. Governing equations and variational formulation

Buoyancy-driven convection is considered here for low inertia flow through saturated homogeneous porous media (see e.g. Nield and Bejan, 1999). Under these assumptions, the momentum equation may be simplified to the standard form of Darcy's law relating the filtration velocity to the pressure gradient and body force term. The flow is assumed incompressible and the Boussinesq approximation for density ρ is employed in the momentum equation.

Conservation of energy is modeled by a single equation requiring the specification of an effective heat capacity and thermal conductivity since energy transfer occurs in both phases. Since the solute does not interact with the solid, the fluid velocity rather than the filtration velocity appears in the convective terms of the solute transport equation and the porosity enters as a material parameter (see e.g. Gray, 1975). In many applications, an effective solute diffusivity must be defined to account for the effect of the tortuous path in the solid matrix (Wooding, 1959). The resulting dimensional governing equations modeling the coupled transport process are then:

$$\nabla \cdot \boldsymbol{u} = 0 \tag{1}$$

$$\boldsymbol{u} + \frac{\boldsymbol{K}}{\mu}(\nabla p - \rho \boldsymbol{g}) = 0 \tag{2}$$

$$\sigma \frac{\partial T}{\partial t} + \boldsymbol{u} \cdot \nabla T - \kappa_T \nabla^2 T = 0 \tag{3}$$

$$\phi \frac{\partial S}{\partial t} + \boldsymbol{u} \cdot \nabla S - \kappa_S \nabla^2 S = 0 \tag{4}$$

$$\rho = \rho_0[1 - \alpha(T - T_0) + \beta(S - S_0)] \tag{5}$$

where $\boldsymbol{u}$ is the velocity, T is the temperature, S is the solute concentration, and p is the pressure. The absolute viscosity of the fluid is μ, ρ is the density of the fluid, and $\boldsymbol{g}$ is the gravitational acceleration vector. In many porous media, it is often the case that the permeability varies in space or is anisotropic. The permeability in equation (2) has been written as a tensor $\boldsymbol{K}$ for generality with the case of constant isotropic permeability easily recovered. Here we will assume that $\boldsymbol{K} := K\hat{\boldsymbol{K}}$, where K is a dimensional permeability scale, and $\hat{\boldsymbol{K}}$ is a non-dimensional possibly spatially varying tensor.

In equation (3), κ_T is the "effective" thermal diffusivity of the saturated medium $(K_T := k_m/(\rho_0 = c)_f)$ where the subscript m denotes a property associated with the saturated porous medium, and the subscript f refers to a property of the fluid. The parameter c in the definition of κ_T denotes the specific heat per unit volume, and k is the thermal conductivity. The parameter σ is the ratio of the heat capacity of the medium to that of the fluid, $\sigma := (\rho_0 = c)_m/(\rho_0 c)_f$, and ϕ is the porosity. The effective solute diffusivity is denoted by K_S. In the body force term of equation (2) the fluid density ρ is modeled (under the Boussinesq assumption) as the linear function of temperature and concentration given by equation. (5), where α is the thermal expansion coefficient and β is the solute expansion coefficient. The subscript zero denotes a reference value of density, temperature, or solution concentration.

Appropriate length, time, velocity, temperature, and solute concentration scales are used to define the non-dimensional variables:

$$\boldsymbol{x}^* := \frac{\boldsymbol{x}}{d}, \quad t^* := \frac{t}{\sigma d^2/K_T}, \quad \boldsymbol{u}^* := \frac{\boldsymbol{u}}{K_T/d},$$
$$T^* := \frac{T - T_0}{\Delta T}, \quad S^* := \frac{S - S_0}{\Delta S}, \quad p^* := \frac{K}{\mu K_T} p$$

where d is a characteristic length scale (such as the height of a porous medium layer) and the thermal and solute concentration scales ΔT and ΔS are chosen so that $0 \leq T^*, S^* \leq 1$. Equations (1-4) in non-dimensional form become (dropping the * for convenience and substituting $\boldsymbol{u}$ from equation (2) into equations (1), (3) and (4)):

$$\nabla \cdot \left(\hat{\boldsymbol{K}}(\boldsymbol{b} - \nabla p)\right) = 0 \tag{6}$$

$$\frac{\partial T}{\partial t} + \hat{\boldsymbol{K}}(\boldsymbol{b} - \nabla p) \cdot \nabla T - \nabla^2 T = 0 \tag{7}$$

$$\frac{\phi}{\sigma}\frac{\partial S}{\partial t} + \hat{\boldsymbol{K}}(\boldsymbol{b} - \nabla p) \cdot \nabla S - \kappa \nabla^2 S = 0 \tag{8}$$

where $\kappa := K_S/K_T$ is the ratio of the solutal and thermal diffusivities and $\boldsymbol{b} := (\kappa R_S S - R_T T)\hat{e}_g$ is the buoyant force vector, with $R_T := g\alpha K \Delta T d/\nu K_T$, the thermal Rayleigh number, and $R_S := g\beta K \Delta S d/\nu K_S$, the solute Rayleigh number. The kinematic viscosity of the fluid is denoted by $\nu := \mu/\rho_0$, and the magnitude of the gravitational acceleration is $g := |\boldsymbol{g}|$. Gravity acts in the direction described by the unit vector $\hat{e}_g$. Equations (6)-(8) will be used in the variational formulation (section 2) and finite element discretization (section 3) described subsequently. Equation (6) can essentially be viewed as a constraint equation for the coupled pair of advection-diffusion equations (7) and (8).

In the application class of interest, heat diffuses much more quickly than mass, which implies $\kappa \ll 1$ and the solute transport equation has a singular perturbation structure. This structure implies that thin boundary layers may form in the solute solution profile, and this motivates the need for adaptive mesh refinement and multi-resolution simulation. The further presence of the convective term suggests that fictitious numerical oscillations may be generated on coarser meshes during the adaptive process and hence a stabilized scheme would further improve the robustness of the associated algorithm as described later (section 3).

An auxiliary non-dimensional group which appears in the literature is the buoyancy ratio $N := \beta \Delta C/\alpha \Delta T$, which is a measure of the competing solutal and thermal buoyancy effects. In this work we have chosen the sign convention in equation (5) which yields $\alpha, \beta > 0$ and therefore $N > 0$. This is consistent with the configuration of competing thermal and solutal layers considered in later simulation studies. In addition, it is common in the literature to use the Lewis number $Le := \kappa^{-1}$. The relationship between these dimensionless parameters is then given by $R_T N Le = R_S$.

A corresponding weak variational formulation on the domain Ω may be constructed in the usual weighted-residual manner by projecting residuals for equations (6)-(8)

against spaces defined by admissible test functions $v_p \in V_p, v_T \in V_T$, and $v_S \in V_S$, respectively, and applying the divergence theorem to obtain

$$\int_\Omega \hat{\boldsymbol{K}}(\boldsymbol{b} - \nabla p) \cdot \nabla v_p \, dx = \int_{\partial\Omega} \left(\hat{\boldsymbol{K}}[\boldsymbol{b} - \nabla p] \cdot \hat{n}\right) v_p \, ds \tag{9}$$

$$\int_\Omega \left(\frac{\partial T}{\partial t} + \hat{\boldsymbol{K}}(\boldsymbol{b} - \nabla p) \cdot \nabla T\right) v_T + \nabla T \cdot \nabla v_T \, dx = \int_{\partial\Omega} (\nabla T \cdot \hat{n}) v_T \, ds \tag{10}$$

$$\int_\Omega \left(\frac{\phi}{\sigma}\frac{\partial S}{\partial t} + \hat{\boldsymbol{K}}(\boldsymbol{b} - \nabla p) \cdot \nabla S\right) v_S + \kappa \nabla S \cdot \nabla v_S \, dx$$
$$= \int_{\partial\Omega} \kappa(\nabla S \cdot \hat{n}) = v_S \, ds \tag{11}$$

where $\partial\Omega$ is the boundary of Ω and $\hat{n}$ is the outward unit normal vector. We note that for a homogeneous isotropic permeability, $\hat{\boldsymbol{K}}$ would become the $n_{sd} \times n_{sd}$ identity matrix, where n_{sd} is the number of space dimensions.

Essential boundary conditions may be included explicitly by restricting the class of admissible solution functions. This implies that the corresponding test functions are zero on those portions of the boundary, and therefore these boundary integral contributions vanish. Penalty approaches are also popular strategies for weakly enforcing essential conditions.

Any remaining flux (Neumann) boundary conditions can be incorporated as natural boundary conditions by simply substituting the desired flux data in the boundary integrals on the right-hand side of the above equations. For example, in equations (9) for the pressure, no flow normal to an impermeable wall $(\boldsymbol{u} \cdot \hat{n} = 0)$ can be enforced in a weak sense by setting the corresponding expression in the boundary integrand on the right to zero.

Finally, since only the gradient of the pressure appears in equations (9)-(11) it is clear that, when Neumann-only boundary conditions are provided in equation (9), the pressure is only specified up to an arbitrary constant. The indefiniteness of the system is, in general, not a difficulty for iterative Krylov subspace solvers when they are given a reasonable initial guess. However, some preconditioners, such as e.g. ILU(0), are less robust in the presence of indefinite systems and for this reason we typically ensure that the system is definite by pinning a specific value of the pressure at an arbitrary node on the boundary.

3. Discretization scheme

A Galerkin finite element approximate formulation is constructed by posing the previous weak statement on a finite element discretization of domain Ω with associated finite-dimensional approximation spaces $V_p^h \subset V_p$, $V_T^h \subset V_T$, $V_S^h \subset V_S$. In this work, standard Lagrange finite element basis functions, $\{\varphi_i\}, i = 1, \ldots, N$ are used. The dependent variables (p, T, S) are approximated by semi-discrete expansions (p^h, T^h, S^h) in the usual manner (see e.g. Becker 1981; Gallagher *et al.*, 1984; Gresho and Sani, 1998; Hughes, 1987; Strang and Fix, 1973; Johnson, 1987).

For small values of κ, the standard Galerkin method may produce oscillatory solutions to convection-dominated transport if the mesh is not sufficiently fine. AMR may be able to solve this problem, but we are also interested here in enhancing the reliability and efficiency of AMR via stabilization. More specifically, stabilization will help maintain robust algorithms on coarse and intermediate meshes during AMR and coarsening. In fact, coarsening during the AMR process may otherwise induce local oscillations that degrade the reliability of the non-linear solver, and in turn trigger undesirable additional refinement.

Hence, to ameliorate this difficulty and enhance algorithm reliability on fixed meshes or on intermediate adaptive meshes, a consistent stabilizing term is included that is proportional to the solute equation residual given in equations (8). The stabilized Galerkin method is then: find p^h, T^h and S^h, satisfying the boundary and initial conditions, such that

$$\int_{\Omega} \hat{\boldsymbol{K}}\left(\boldsymbol{b}^h - \nabla p^h\right) \cdot \nabla v_p^h \, dx = \int_{\partial\Omega} \left(\hat{\boldsymbol{K}}\left[\boldsymbol{b}^h - \nabla p^h\right] \cdot \hat{n}\right) v_p^h \, ds \tag{12}$$

$$\begin{aligned} &\int_{\Omega} \left(\frac{\partial T^h}{\partial t} + \hat{\boldsymbol{K}}\left(\boldsymbol{b}^h - \nabla p^h\right) \cdot \nabla T^h\right) v_T^h + \nabla T^h \cdot \nabla v_T^h \, dx \\ &\quad = \int_{\partial\Omega} (\nabla T^h \cdot \hat{n}) v_T^h ds \end{aligned} \tag{13}$$

$$\begin{aligned} &\int_{\Omega} \left(\frac{\phi}{\sigma}\frac{\partial S^h}{\partial t} + \hat{\boldsymbol{K}}\left(\boldsymbol{b}^h - \nabla p^h\right) \cdot \nabla S^h\right) v_S^h + \kappa \nabla S^h \cdot \nabla v_S^h \, dx \\ &\quad + \int_{\Omega'} \tau_e \left(\hat{\boldsymbol{K}}\left(\boldsymbol{b}^h - \nabla p^h\right) \cdot \nabla v_S^h\right) \mathscr{R}_S^h \, dx = \int_{\partial\Omega} \kappa (\nabla S \cdot \hat{n}) v_S^h \, ds \end{aligned} \tag{14}$$

holds for every admissible v_p^h, v_T^h and v_S^h. Here,

$$\mathscr{R}_S^h := \frac{\phi}{\sigma}\frac{\partial S^h}{\partial t} + \hat{\boldsymbol{K}}\left(\boldsymbol{b}^h - \nabla p^h\right) \cdot \nabla S^h - \kappa \nabla^2 S^h \tag{15}$$

is the strong-form solute equation residual (equation (8)) for the finite element approximation, τ_e is an element-wise stabilization parameter, and the stabilization integral is defined over Ω', the union of element interiors. Equation (14) is an extension of the classical SUPG stabilization scheme (Brooks and Hughes, 1982) for a nonlinear advection-diffusion equation. We note that the additional term has been designed in a consistent manner, in that it vanishes (by equation (8)) upon substitution of the exact solution. In this particular problem, both the stabilization parameter τ_e and the upwind-modified weighting function $\hat{\boldsymbol{K}}(\boldsymbol{b}^h - \nabla p^h) \cdot \nabla v_S^h$ depend on the unknown solution.

While the exact form of τ_e for the one-dimensional linear advection-diffusion equation is well-known, for higher-dimensional problems in which strongly-nonlinear velocity fields and source terms are present, designing τ_e is a non-trivial task. The main difficultly lies in adding enough artificial dissipation to suppress spurious oscillations in the solution without degrading the overall (asymptotic) accuracy of the method in the process. In the present work, we use the following form of τ_e (based on the work in shakib, 1991)

$$\tau_e := \left[\left(\frac{\partial \xi_i}{\partial x_j}\frac{\partial \xi_i}{\partial x_k}\right) u_j u_k + \kappa^2 \left(\frac{\partial \xi_i}{\partial x_k}\frac{\partial \xi_j}{\partial x_k}\frac{\partial \xi_j}{\partial x_l}\frac{\partial \xi_i}{\partial x_l}\right)\right]^{-1/2} \tag{16}$$

in equation (14), where u_i is the ith component of the velocity field, summation over repeated indices *i, j, k* and *l* is implied, and where $\partial\xi_i/\partial x_j$ is the (*i, j*) entry of the inverse

Jacobian of the geometric map between the reference element and physical element Ω_e. The entries in the inverse Jacobian matrix are $\mathcal{O}(h_e^{-1})$, where h_e is a characteristic size of the physical element Ω_e. We remark that this particular choice of τ_e reduces in the 1D, constant-velocity case to

$$\tau_e = \frac{h_e}{2|\boldsymbol{u}|}\left(\sqrt{\frac{\alpha^2}{1+\alpha^2}}\right) \tag{17}$$

where $\alpha := h_e|\boldsymbol{u}|/2\kappa$ is the cell Peclet number. Although this simplified form is not directly applicable to the present problem, it is instructive because it shows that τ_e has the correct $\mathcal{O}(h_e)$ asymptotic dependence on the mesh spacing.

The stabilized Galerkin method of equations (12)-(14) yields a semi-discrete system of coupled non-linear differential algebraic equations. To integrate from time level t^n to t^{n+1}, where $t^{n+1} := t^n + \Delta t$, a standard θ-scheme is applied (Smith, 1996). The method is formally second-order accurate in time if $\theta = 1/2$, and the steady equations are recovered in the code by setting $1/\Delta t := 0$ and $\theta := 1$. For oscillatory transient problems we use the second-order time differencing scheme. In the steady-state continuation problems, both time-stepping and steady-state solves are combined in an innovative manner as described later in Algorithm 1. The resulting fully discrete non-linear system of equations is solved here via an inexact Newton method. The Jacobian entries for the non-linear system are precomputed analytically, with the exception of the derivatives of the stabilization parameter τ_e with respect to the dependent variables, which are handled more effectively via finite differences due to their complexity.

4. Solution algorithm and AMR implementation

The solution scheme is designed to allow accurate computations in and investigations of challenging parameter regimes. The general idea is to combine both time stepping and continuation techniques to arrive at stable solutions to advection-dominated problems on grids which are highly-refined in layers or regions of interest. This method allows us to retain the benefits of AMR without the excessive computational costs that may be involved in adapting at every timestep. In addition, it provides a reasonable procedure for stepping through a given region of parameter space, and gradually increasing (resp. decreasing) the problem size as the solutions become more (resp. less) challenging. Algorithm 1 describes the process used to generate sequences of solutions and map the parametric space.

4.1 AMR error indicator

AMR (*h*-refinement) has been used to generate efficient well-graded grids in multi-resolution problems for many years, and there is a rich literature in the areas of computable error indicators (Zienkiewicz and Zhu, 1987; Bangerth and Rannacher, 2003), theoretical a posteriori error estimates (Ainsworth and Oden, 2000; Babuška and Rheinboldt, 1978), and application studies which use *h*-refinement as an essential ingredient in the overall solution scheme (Carey *et al.*, 2004; Anderson *et al.*, 2005). In this work, we employ a flux-jump error indicator similar to the classical indicator proposed by Kelly *et al.* (1983) to drive the *h*-refinement process.

Following the previous line of multiscale reasoning (related to the size of κ) which led to stabilization of the solute equation, the solute approximation is also used to construct an error indicator to drive the adaptivity process in the fully coupled solution algorithm. We recognize that, in general, the use of a single solution component to drive the adaptivity process may not be sufficient to control the pollution error arising from other components of a coupled physical system. In such cases, the use of weighted linear combinations of error indicators, and adjoint methods which assess the sensitivity and influence of the error on quantities of interest, may be required as well. These and related techniques are topics of recent and ongoing research (Carey *et al.*, 2009; Estep, 2008).

Algorithm 1: The AMR/continuation solution scheme: First, select a generic parameter "χ" (e.g. $\chi = \kappa, R_T, R_S$, etc.) and a "moderate" initial value χ_0. Then solve the unsteady equations starting from a given initial condition, e.g. the linear conducting state. AMR is not active during this time-dependent evolution stage. Once steady state is detected for χ_0, we increment χ and begin the steady solve continuation loop. The AMR process is driven by the flux-based indicator of equation (18) and the statistical flagging scheme mentioned in section 4. The initial guess to the iterative non-linear solver at each step is the solution at the previous parameter value, projected onto a newly, refined grid.

```
Initialize, set $\chi = \chi_0$.
Solve unsteady equations to steady state (AMR inactive).
Increment $\chi$.
while $\chi \neq \chi_f$ do
    Solve steady equations for current $\chi$.
    Adaptively refine/coarsen the grid, project the solution, and re-solve.
    Increment $\chi$.
end while
```

In the subsequent AMR simulations, we compute the solute flux jump error indicator for a given element *e* with boundary $\partial\Omega_e$ as

$$\eta_e^{\mathrm{FLUX}} := \left(\frac{h_e}{24} \int_{\partial\Omega_e} |R_e|^2 ds \right)^{1/2} \tag{18}$$

where the interface residual is

$$R_e := \begin{cases} 0, & \in \Gamma_D \\ g_N - \nabla S^h \cdot \hat{n}_e, & \in \Gamma_N \\ \frac{1}{2}(\nabla S^h|_f - \nabla S^h|_e) \cdot \hat{n}_e, & \in \partial\Omega_e \cap \partial\Omega_f \neq \emptyset \end{cases} \tag{19}$$

Here Γ_D and Γ_N are the Dirichlet and Neumann boundary segments for the solute variable, g_N represents given Neumann boundary data, $\hat{n}_e$ is the outward unit normal for cell *e*, and cell *f* shares an edge (face) with cell *e* in the finite element mesh. In regions of rapidly changing solution gradient (such as in boundary or internal layers) this term will be large and hence refinement will be triggered in such zones.

Another important aspect of AMR is the manner in which one uses the computed error indicator to actually flag individual elements for refinement and coarsening. Statistical approaches are fairly robust (Carey and Humphrey, 1981; Aftosmis and Berger, 2002; Peterson *et al.*, 2007) and in this work we employ such a strategy, treating the element error as an approximately log-normal distribution and flagging elements in the tails for refinement/coarsening. Additional stopping tests are applied in the full algorithm.

4.2 The `LibMesh` library

The main solution steps in Algorithm 1 are accomplished using the `LibMesh` (Kirk, 2006) software library developed primarily by our CFD research group over the past several years. `LibMesh` is designed to facilitate parallel, adaptive multiphysics/multiscale simulations using adaptive mesh strategies and finite element approximation schemes. The software is written in C++ and takes advantage of object-oriented design features to enable use across different application domains and to facilitate coupling with independent libraries such as `ParMETIS` (Karypis and Kumar, 1998) for parallel partitioning and `PETSc` (Balay *et al.*, 1997) for iterative solvers. `LibMesh` is an open source software package available to the scientific community via the Sourceforge.net (`http://libmesh.sf.net`) site. The design of `LibMesh` has been influenced by the scientific and engineering communities' need for large-scale, coupled, multi-resolution simulation capability. Object-oriented programming techniques pioneered by other research groups (Cross *et al.*, 1999), and the existence of other high-performance C++ finite element libraries such as `deal.II` (Bangerth, 2000), `Alegra` (Budge and J. Peery, 1996), `PZ` (Devloo and Longhin, 2002), and `UG` (Bastian *et al.*, 1997) have also inspired our own research.

Applications employing `LibMesh` are built on top of an existing class library with a well-defined application programming interface (API) that provides the infrastructure for the parallel adaptive capability. Parallelism is achieved via domain decomposition to mesh subdomains that are distributed across the available processors. Elements are wholly owned by processors while nodes on common subdomain interfaces are assigned to the processor with lower global index. The resulting data structure enables efficient communication across the distributed processors.

As described earlier, the adaptive mesh refinement strategy involves subdivision of parent elements and their children to define an unbalanced tree data structure. Continuity requirements across edges between refined and unrefined cells (that is cells at different levels in the tree) are treated here algebraically using interfacial constraints. Discontinuous approximations with weak interfacial constraint enforcement (Discontinuous Galerkin schemes) have also been implemented within the `LibMesh` library. The adaptively refined grids shown later are composed of either quadrilateral/triangular (2D) or hexahedral/tetrahedral (3D) geometric element types.

We now briefly discuss a few key aspects of the techniques used to enforce C^0-continuity across the non-conforming (so-called "hanging node") edges and faces present in all the adaptively refined meshes used in this work. In the `LibMesh` library, we have taken special care to ensure that the computation of hanging node constraints is an efficient, data-local, geometric-element-type-independent procedure. C^0-continuity is enforced in the following manner: we let u^F and u^C be the fine and coarse scale finite element solutions, respectively, and assume u^F is to be constrained to u^C along some shared interface, γ. Then, we impose

$$(u^F, \phi_k^F)_\gamma = (u^C, \phi_k^F)_\gamma \quad \forall\, k = 1, \ldots, N_F \tag{20}$$

where $(\cdot,\cdot)_\gamma$ is the standard L_2 inner product on γ, ϕ_k^F is the fine scale basis function associated to degree of freedom k, and N_F is the number of fine scale basis functions. Expanding the finite element solutions in their appropriate bases eventually leads to the (small) linear system of equations

$$Au^F = Bu^C \tag{21}$$

We can then solve for the fine degrees of freedom by numerically inverting the square matrix A. To improve the data locality of the scheme, we assume always that a conforming "level-0" coarse mesh exists and that child degrees of freedom can be constrained to a parent's degrees of freedom, rather than a neighbor's.

This idea is illustrated in Figure 1(a), in which the hanging node (black dot in the figure) constrains the refined elements A, B, and C to take on the mid-edge value of neighboring element D at this point. In the `LibMesh` library, to minimize potential communication overhead, we would instead constrain the hanging node on element A to the value on its parent element P, as shown in Figure 1(b). We know element P exists due to the conforming grid assumption, and element A has $\mathcal{O}(1)$ look-up time for its parent due to the natural structure of the refinement tree. The hanging node value can then be constrained simply by considering the finite element solution space of the parent as the "coarse" space. The neighboring element is no longer involved, and the L_2 constraint equations now apply to child and parent rather than to the child and coarse neighbor. In cases where more than one refinement level separates neighboring elements (meshes violating the so-called "level-1" rule) the same procedure can be applied; we exploit the fact that the grid is still conforming at some level, and therefore the constraints can be applied recursively.

`LibMesh` also supports spectral degree (uniform *p*) refinement, although fully-automatic *hp*-refinement, in particular the efficient automatic selection of *h* or *p* refinement, remains a topic of ongoing research (Bangerth and O. Kayser-Herold, 2008; Solin and Demkowicz, 2004). The present work exploits the coarsening capability afforded by the refinement tree data structure. That is, active refined cells in the tree can be coarsened to reactivate a parent element. This allows coarsening down to the level of the original mesh. Further details of the AMR data structures, iterative solutions on adapted grids, and other related aspects for parallel adaptive FE simulation are available in Carey (1997) and other sources.

5. Results and discussion

Results for several case studies in two and three dimensions are described for simulations using the stabilized adaptive finite element formulation described in section 3. More specifically, in section 5.1 we investigate the classical heated layer configuration for double-diffusive convection in unit aspect ratio domains for two and three dimensions. This includes a representative study of the oscillatory behavior of the "diffusive" mode, and a more detailed comparison of adaptive and uniform grid results for steady convection in a computationally-challenging diffusivity ratio (Lewis number) regime. These cases are useful as verification tests of the numerical scheme. In section 5.2 a 2D simple enclosure with a "barrier" of lower permeability than the surrounding porous medium is used to further demonstrate utilization of adaptivity. Finally, in section 5.3 we discuss simulations with more complex, 3D geometries.

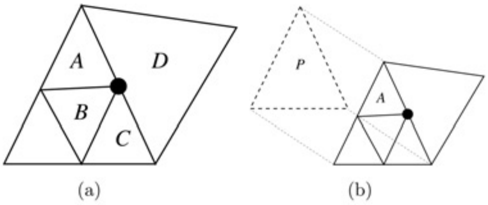

(a) (b)

Notes: (a) Neighbor constraint and (b) parent constraint

Figure 1.
Hanging node (black dot) constraints based on neighbors 1(a) and based on parents 1(b)

Of particular engineering interest in many applications, and requiring accurate resolution of boundary layers, are the Nusselt number N_T and the Sherwood number N_S, defined by

$$N_T := -\int_{\partial\Omega_D} \nabla T \cdot \hat{n}\, dx \quad N_S := -\int_{\partial\Omega_D} \nabla S \cdot \hat{n}\, dx \tag{22}$$

respectively, where $\partial\Omega_D$ is a subset of $\partial\Omega$ for which Dirichlet boundary conditions are specified on the solute. In the results which follow, localized adaptive refinement near the walls is seen to be an effective procedure for improving approximation of these quantities without greatly increasing the size of the global system of equations. The flux calculations can be further improved by applying superconvergent flux post-processing formulae such as those found in (Carey *et al.*, 1985; Pehlivanov *et al.*, 1992). Finally, some problems have analytical results for the relationship between κ and N_S in asymptotic regimes, and these results can be used to verify the numerical results.

5.1 Generalized Horton-Rogers-Lapwood problem

A rich literature exists in the area of double-diffusive convection in porous media (see e.g. Nield and Bejan, 1999, for a list of references). Much of the early work involved analytical investigations and focused on the development of linear stability theory. The classical problem of single-component flow in a thin, heated, isotropic porous medium is referred to as the Horton-Rogers-Lapwood problem. When the layer is heated from below, linear stability theory predicts a critical thermal Rayleigh number of $R_T = 4\pi^2$. Below this value, the linearly stratified quiescent initial state is a stable solution, while above it small disturbances grow, leading to steady convection.

In the double-diffusive case with opposing thermal and concentration gradients, the stability behavior is more complicated. Linear stability theory predicts both steady and oscillatory onset for the layer heated from below with a stabilizing concentration gradient. The critical thermal Rayleigh number for stationary onset is given by

$$R_{T,crit} = 4\pi^2 + R_S \tag{23}$$

The criterion for steady onset only depends on the solutal Rayleigh number, R_S. For oscillatory onset, the stability criterion also depends on the value of

$$\Phi := \frac{\phi}{\sigma} Le \tag{24}$$

The critical Rayleigh number in the oscillatory instability case is

$$R_{T,osc} = 4\pi^2 \frac{1+\Phi}{\Phi} + \frac{R_S}{\Phi} \tag{25}$$

The oscillatory instability is associated with a non-zero imaginary part of the temporal eigenvalue. The linear stability diagram for the quadrant where R_T and R_S are both positive is shown in Figure 2 for a representative value of $\Phi = 10/3$. Note that for $\Phi =\leq 1$, linear theory predicts that only steady onset of convection is possible. In the limit as *Le* (resp. Φ) $\rightarrow \infty$, the dashed line in Figure 2 becomes parallel to the R_S axis, and intersects the steady onset line at the point $R_T = 4\pi^2$. Increasing the value of Le (reducing κ) therefore has the effect of shrinking the stability region (below the dashed line) and thus minimizing the stabilizing effect of the solute field. It has been well-established that the oscillatory mode is subcritical (Nield and Bejan, 1999).

For the results presented in this section, the equations were solved in the unit square domain: $(x, z) \in (0, 1) \times (0, 1)$, with gravity vector $\hat{e}_g = (0, -1)$. The initial data corresponds to the quiescent state with opposing linear solute and temperature profiles, given by

$$\begin{aligned} p_{\text{init}} &= R_T\left[T_{\text{bot}}z + \frac{z^2}{2}(T_{\text{top}} - T_{\text{bot}})\right] - \kappa R_S\left[S_{\text{bot}}z + \frac{z^2}{2}(S_{\text{top}} - S_{\text{bot}})\right] \\ T_{\text{init}} &= T_{\text{bot}} + z(T_{\text{top}} - T_{\text{bot}}) \\ S_{\text{init}} &= S_{\text{bot}} + z(S_{\text{top}} - S_{\text{bot}}) \end{aligned}$$

where $T_{\text{bot}} = S_{\text{bot}} = 1, T_{\text{top}} = S_{\text{top}} = 0$. A small initial perturbation of the form

$$\delta_T(x) = A_{\text{pert}} \sin(\pi x) \tag{26}$$

where $A_{\text{pert}} \approx 10^{-4}$ is applied to the temperature field at time $t = 0$ to induce the development of finite amplitude states, rather than computing much longer relying only on the build-up of roundoff error.

5.1.1 Oscillatory onset of convection. To illustrate the oscillatory mode of onset, a simulation was performed for $R_T = 200, R_S = 750, \kappa = 0.1$ and $\Phi = 5.4$. For these parameters, equation (25) yields $R_{T,osc} = 182.8$, so the simulation should be in the oscillatory onset region. For the large R_S value, steady onset is predicted to occur for $R_T = 790$, so there is a large separation between the critical values of the two modes. Figure 3 shows N_T and N_S vs time for this simulation. The 2D calculation was performed on a 40×40 uniform grid of bilinear quadrilateral elements (which is of adequate resolution for this parameter regime) using the second-order time-differencing scheme. The time range in the figure corresponds to an initial window where the perturbation has grown to finite amplitude.

The behavior at early time is the oscillatory "diffusive" mode predicted by linear stability theory. In this regime, the flowfield reverses direction at the frequency

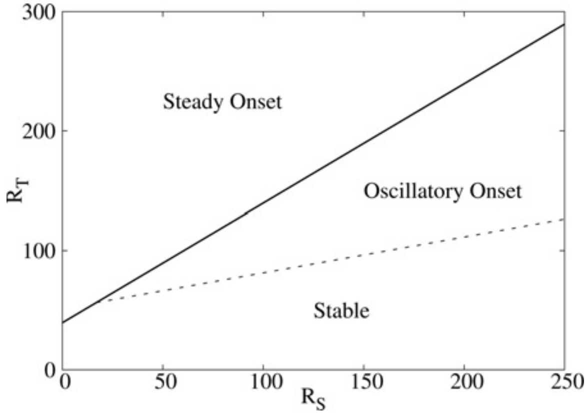

Figure 2.
Linear stability diagram for the destabilizing temperature, stabilizing solute case, with Φ (as defined in equation (24)) equal to 10/3

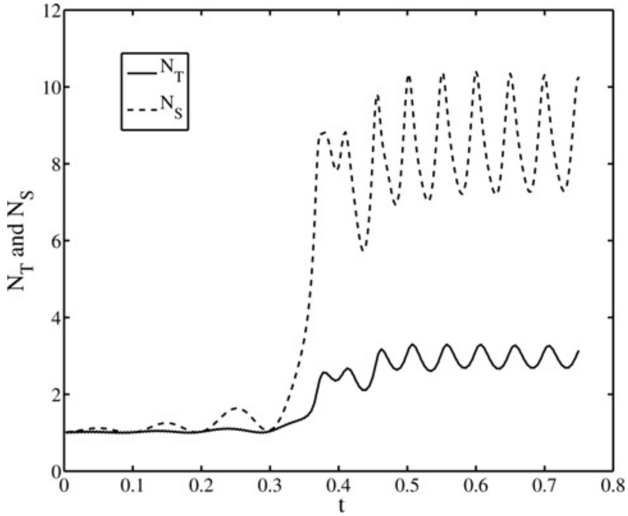

Figure 3.
N_T and N_S as a function of time, for the case $R_T = 200$, $R_S = 750$, $\kappa = 0.1$ and $\Phi = 5.4$

predicted by linear theory (Nield and Bejan, 1999). The values of N_T and N_S grow in an oscillatory manner from the quiescent state value of 1: at a dimensionless time around 0.3, the diffusive mode becomes unstable and there is a large increase in the values of N_T and N_S. For this new convective state the flow cell rotates primarily in one direction but displays secondary oscillations. The nature of the secondary transient flow state depends strongly on the value of κ. There is a broad range of behavior exhibited by these transient subcritical flow states and both time and spatial accuracy are very important in characterizing the various flow states that can occur.

5.1.2 AMR investigation of steady onset. The emphasis in the current study is on steady double-diffusive convection in order to focus on the application of h-adaptive methods. To demonstrate the ability of the adaptive grids in computing steady, double-diffusive convection solutions, we conducted a grid convergence study using the continuation method discussed in section 4. The diffusivity ratio κ was selected as the continuation parameter, and a sequence of solutions was computed starting with a moderate value of $\kappa = 0.1$ and decreasing to the desired value of $\kappa = 0.03(Le = 100/3)$ according to Algorithm 1. The remaining problem parameters were chosen as $R_T = 200, R_S = 160$ and $\phi/\sigma = 1/3$, thus placing us in the regime of steady onset of convection (since $R_T > 4\pi^2 + R_S$). An adaptive grid and three uniform grids containing $40 \times 40, 60 \times 60$, and 150×150 bi-linear quadrilateral elements were compared. (In the uniform grid cases, the refine/coarsen step in Algorithm 1 is simply skipped.) The adaptive grid was initialized with 15×15 coarse-level elements, and a maximum refinement "depth" of four levels was allowed in order to be consistent with the finest mesh resolution studied in the uniform case.

A perturbation is applied to the initial quiescent state as described above. For this set of computations it is advantageous to supply an initial perturbation in order to guarantee which segment of the x-periodic solution (e.g. central upwelling or central downwelling) is obtained. Use of the perturbation form given in equation (26) always produces the solute upwelling solution shown in Figure 4. The steep boundary layers present in the solute field for this value of κ are apparent in Figure 4(a) near the top and bottom Dirichlet boundaries. In the interior of the domain, a thin solute layer of

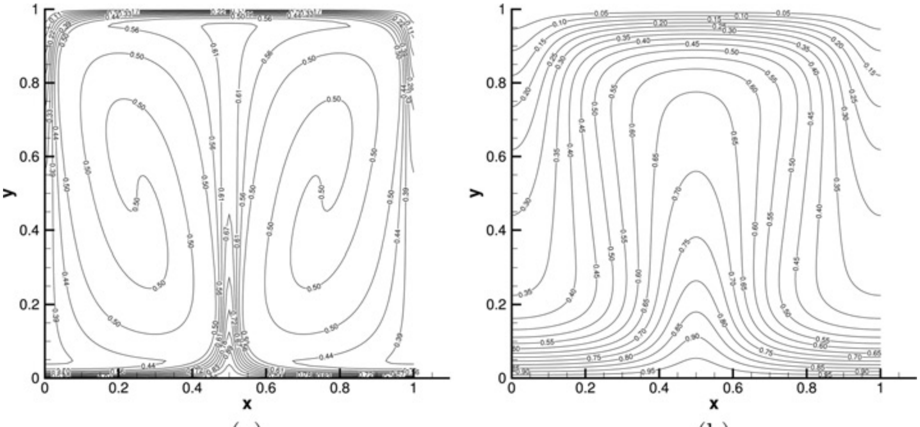

(a) (b)

Figure 4.
Contours of solute (Figure 4(a)) and temperature (Figure 4(b)) for $\kappa = 0.03$ on reference uniform 150×150 grid

Notes: (a) Solute contours and (b) temperature contours

approximately the same width rises up from the bottom boundary. Accurate calculation of the Sherwood number depends strongly on carefully capturing these solution features.

In contrast, the thermal field (shown in Figure 4(b)) does not contain sharp boundary layers. This behavior is quite typical for this class of applications, and justifies the decision to allow adaptive refinement to be driven entirely by the solute field. In this case, the true solution is not known, so we give our comparisons relative to the most-refined uniform grid with 150×150 elements (151×151 nodes, three degrees of freedom (dofs) per node, for a total of 68,403 dofs).

A plot of $S(y)$ along the line $x = 0.5$ (shown schematically in Figure 5(a)) for several different grids is given in Figure 6(a). Grid convergence of the solutions is demonstrated

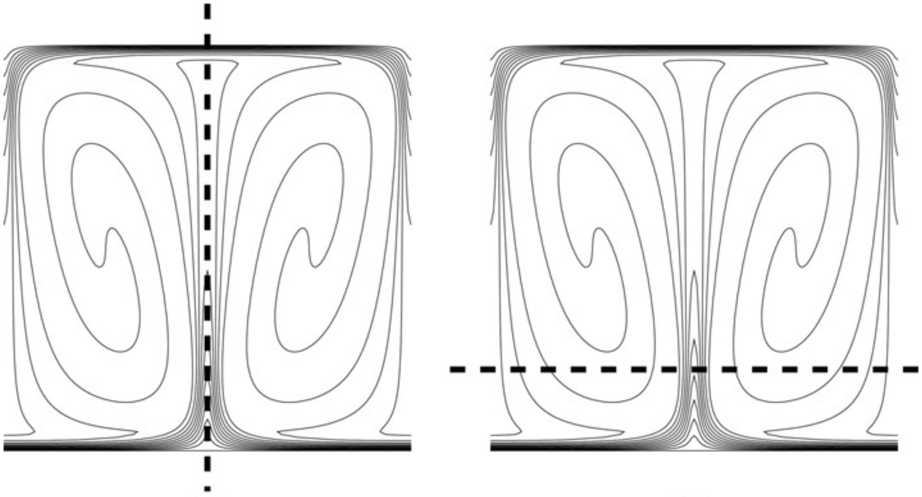

(a) (b)

Figure 5.
Location of slices for line plots

Notes: (a) Location of $x = 0.5$ slice and (b) location of $y = 0.2$ slice

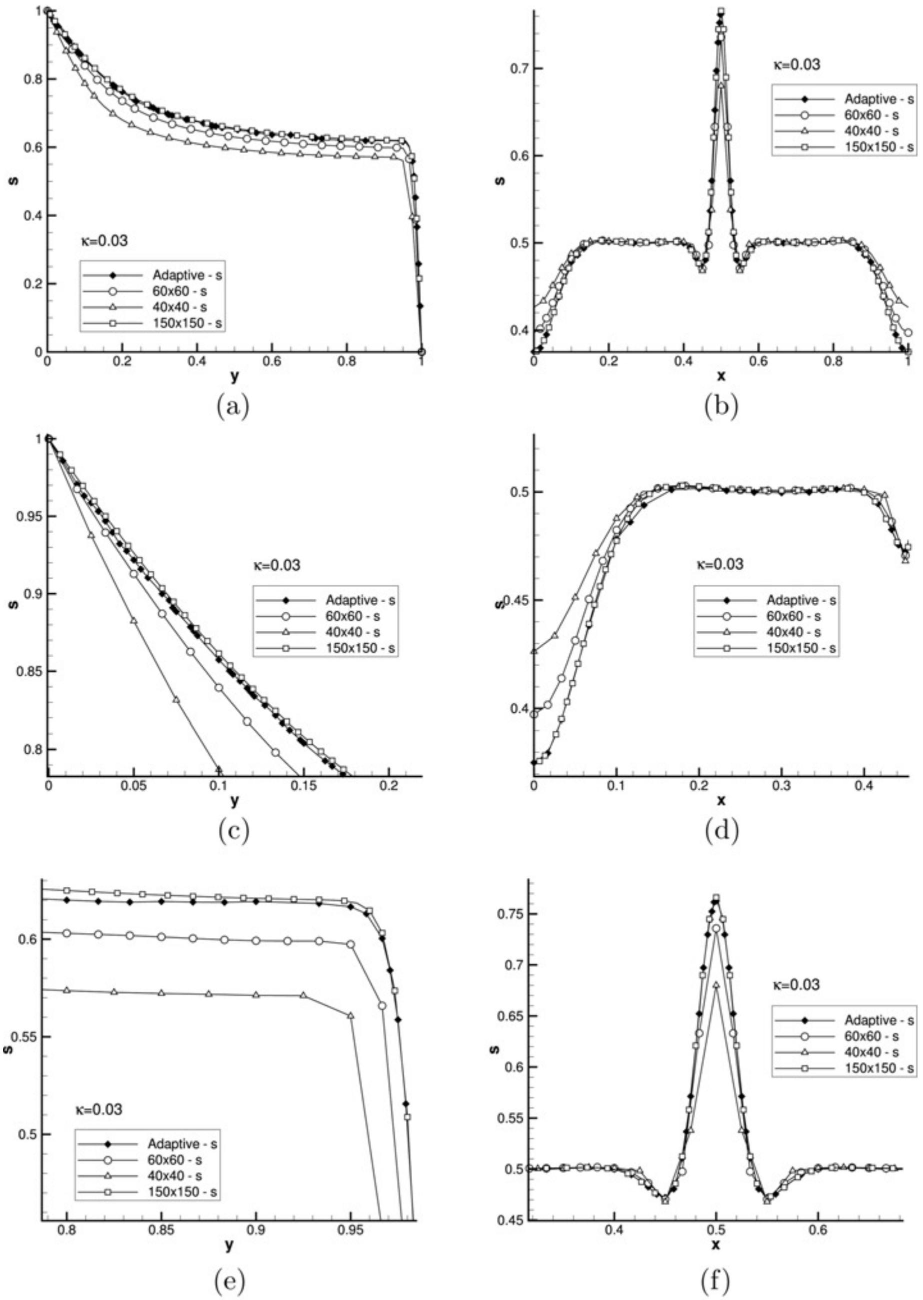

Figure 6.
Comparison of line plots of solute concentration with $\kappa = 0.03$ for the adaptive (◆), 150 × 150 (□), 60 × 60 (○), and 40 × 40 (△) grids

Notes: (a) $S(y)$ along the line $x = 0.5$, (b) $S(x)$ along the line $y = 0.2$, (c) $S(y)$ along the line $x = 0.5$ near $y = 0$, (d) $S(x)$ along the line $y = 0.2$ near $x = 0$, (e) $S(y)$ along the line $x = 0.5$ near $y = 1$, and (f) $S(x)$ along the line $y = 0.2$ near $x = 0.5$

in the line plots of the solute variable given in Figure 6. The sharpness of the solute boundary layer near $y = 1$ is readily observed in this plot. Close-up views of the line plot in Figure 6(a) near $y = 0$ and $y = 1$ are given in Figures. 6(c) and 6(e), respectively. These plots reveal that the solutions on the 40×40 and 60×60 grids are stable, but overly diffuse, relative to the fine 150×150 uniform grid solution. This arises from the artificial diffusion introduced by the SUPG formulation. The Sherwood number is under-predicted on these coarse grids because of the added diffusion, but this is generally preferable to the node-to-node oscillations which would be present in the absence of stabilization on an ungraded mesh. Excellent agreement in the boundary layer region is observed between the adaptive grid and the finest uniform grid solutions considered. However, the adapted grid (shown in Figure 7(a)) contains approximately 50 per cent fewer nodes.

In order to demonstrate the capability of the adaptive grids near insulated boundaries and internal layers, we have also included line plots of the solute variable along the line $y = 0.2$ shown schematically in Figure 5(b). Figure 6(b) gives a comparison along this line for several different grids. A close-up of the near-wall region, given in Figure 6(d), once again reveals good agreement between the adapted and uniform 150×150 grids while showing that the coarser grids tend to over-predict the solute value in this region. A close-up of the internal layer near $x = 0.5$ is given in Figure 6(f). Here, the coarse grid solutions are oscillation-free but tend to under-predict the maximum solute value along the centerline. The adapted grid has a highly localized refinement pattern in this region, and the solution is in good agreement with the 150×150 reference solution.

It is imperative to stress that these convergence results imply only that the uniform and adaptive grid calculations are converging stably to the same solution, which is not to say that they will be in good agreement with independent theoretical, experimental, or numerical results. We now endeavor to show that our results are also in agreement with asymptotic boundary layer theory for porous media layers.

Based on analytical asymptotic theory and numerical computations in porous media boundary layers (Bejan, 1984; Bejan and Khair, 1985; Angirasa and Peterson, 1997) and studies of convection in enclosed porous media (Trevisan and Bejan, 1985, 1986) it is known that the Sherwood number has an asymptotic square root dependence on the thermal Rayleigh number R_T and the Lewis number *Le*

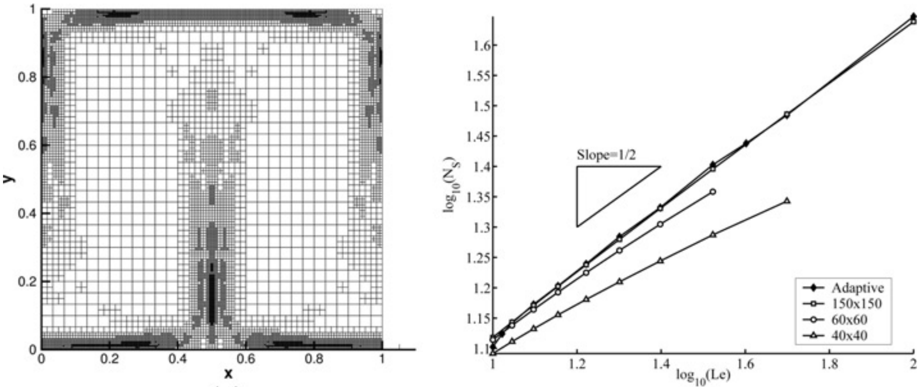

(a) (b)

Figure 7.
Adaptively-refined grid (10,929 nodes, 32,787 dofs) used for comparison in grid convergence study (left, Figures 7(a)). Plot of the log of the computed Sherwood number (N_S) vs the log of the Lewis number (*Le*) for the adaptive (◆), 150×150 (□), 60×60 (○), and 40×40 (△) grids used in the grid convergence study, Figure 7(b), right

Notes: (a) Adapted grid and (b) log *Ns* vs log *Le*

$$N_S \approx \sqrt{R_T Le} = \sqrt{\frac{R_T}{\kappa}} \tag{27}$$

for $Le, R_T \gg 1$. This asymptotic regime is computationally challenging and provides a useful verification test. Accordingly, the Sherwood numbers are computed on the grids previously utilized for decreasing values of κ (resp. increasing *Le*). The other non-dimensional parameters and the initial conditions are the same as before. Figure 7(b) gives a plot of $\log(N_S)$ vs log(*Le*) for $10 \leq Le \leq 100$ for the same grids discussed previously. Since R_T is held constant in this case, we expect an asymptotic square-root dependence of N_S on Le as $Le \rightarrow \infty$. This is indeed observed in Figure 7(b) for the finest uniform grid and the adaptive grid calculations, even for moderate *Le*. The fine uniform and adaptive grid results are therefore consistent with the theoretically predicted asymptotic behavior. The coarse uniform grids, on the other hand, not only under predict the N_S vs. *Le* trend, they also do not exhibit the proper constant-slope behavior, trailing off at the higher (more challenging) *Le* values.

5.1.3 3D analog of the steady onset case. We also investigated an analogous three-dimensional version of the Horton-Rogers-Lapwood problem in a cube. The same physical parameters as in the 2D case were used once again: $R_T = 200$, $R_S = 160$, $\phi/\sigma = 1/3$, and $\kappa = 0.1$. An initial mesh with $20 \times 20 \times 20$ trilinear hexahedral elements was employed in this particular case. Three different views of a representative steady-state 3D solution are shown in Figure 8. Figure 8(a) gives a detailed picture of the post-processed velocity field vectors superimposed on the temperature field. These velocity vectors were computed using the constrained L_2-projection technique described in the Appendix, and show downwelling fluid in the four corners and the top of the domain, with four identical recirculating upwelling regions on each of the side faces of the cube.

In Figure 8(b), we give an "exploded" view of the 3D domain which more clearly shows the sharpness of the solute boundary layers near the top and bottom of the domain. Finally, in Figure 8(c), a representative simple example of a 3D adapted mesh is shown. The adaptivity tracks the solute boundary layers at the top and bottom of the domain, similar to the 2D case discussed previously. Similar improvements (not shown here) in the computation of the solute Nusselt number over uniform grids were achieved for this 3D case as well.

5.2 Variable permeability effects

An important, physically meaningful application of double-diffusive convection modeling concerns the effect that a spatially varying permeability field will have on the flow. Naturally occurring features such as high-permeability vertical streaks (McKibbin 1986) and horizontal cracks (McKibbin and Tyvand, 1984; Debeda *et al.*, 1995) can significantly affect the global flowfield as well as generate extremely localized regions of high temperature and concentration gradients. Here, we consider a simple enclosure with a "barrier" of lower permeability than the surrounding porous medium, and investigate the influence on the flow field. The setup for this configuration is shown in Figure 9(a).

The permeability of the barrier, K_b, is assumed to be a fixed value which is smaller than the permeability of the surrounding medium, K, i.e. $K_b/K < 1$. The identity permeability matrix $\hat{\boldsymbol{K}}$ is diagonally-scaled inside this region. In the first set of experiments, the same physical parameters are used as in the preceding section (with $\kappa = 0.1$) and the geometric parameters $H = 0.1, L = 0.48$, and $t = 0.025$ are selected. Three different values of the permeability ratio, $K_b/K = 10^{-2}, 10^{-3}$, and 10^{-4} are

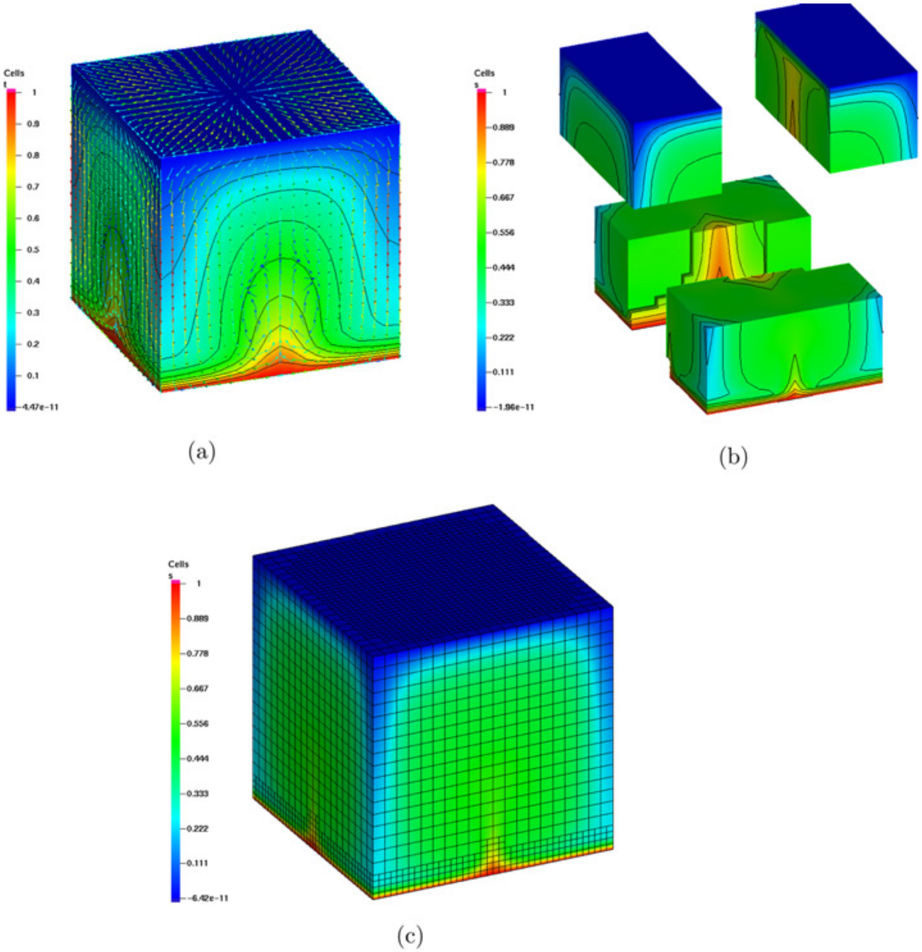

(a) (b) (c)

Figure 8.
The temperature field and velocity vectors (Figure 8(a)) for the 3D analogue of the Horton-Rogers-Lapwood problem in a cube. (The velocities have been projected into a C^0 continuous basis for visualization using the method described in the Appendix.) An exploded view of the solute plume is shown in Figure 8(b). In the exploded view the solute boundary layer which forms at the top of the domain is also clearly visible. Finally, in Figure 8(c), we show the relatively simple adapted mesh for this case. Refinement is concentrated in the boundary layers at the top and bottom of the domain

Notes: (a) Temperature field and velocity vectors, (b) exploded view of solute plume and (c) adapted grid

tested. In order to avoid any permeability "averaging" affects across the discontinuous barrier, the enclosure was meshed so that the element edges aligned exactly with the low-permeability region, as shown in Figure 9(b).

The steady-state solute contours and adapted grids for the three different permeability ratios are shown in Figure 10. In general, we observe that as K_b/K decreases, additional adaptivity is triggered to capture the rapid flow speed transition which occurs near the barrier, especially in the gap between the low-permeability barriers. The adaptivity still tracks the sharp solute boundary layers near the top and bottom of the domain as well.

The presence of the semi-permeable barrier adds interesting detail to the simulation. Three distinct rotating convection cells can be observed: two divided by the solute plume in the bottom of the domain, and one in the top left corner. In the bottom left corner of the domain, there is also a thickening of the solute boundary layer as the

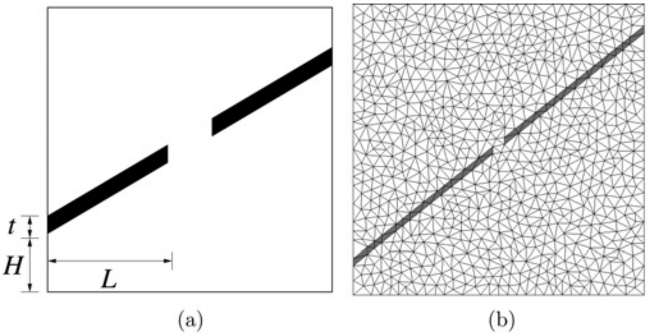

Notes: The left and right sides of the barrier have horizontal length L. The bottom of the barrier begins at height H on the left side of the domain and ends at height $1 - H$ on the right side. The barrier has thickness t throughout. The initial triangulation of an enclosure with parameters $H = 0.1$, $L = 0.48$ and $t = 0.025$ is shown, wth the barrier highlighted in gray, on the right

Figure 9.
Geometric configuration of the slanted semi-permeable barrier problem in the unit square

permeability ratio decreases, due to the proximity of the semi-permeable barrier. The adaptivity therefore does not target this corner for refinement as strongly in the latter two cases. We believe this relatively simple geometry (defined by the three parameters *H, L*, and *t*) provides an additional thermosolutal convection benchmark candidate.

5.3 Double-diffusive convection in complex 3D geometries

A common problem which arises in engineering applications is the double-diffusive natural convection of a fluid around cylindrical objects (i.e. pipes). Hasan and Mujumdar (1985) mention several such applications, including underground nuclear detonation, porous dikes filled with steam and gases from rock vapor, and injection-well oil-recovery techniques. In that study, a shooting method is used to compute 2D solutions to the equations of double-diffusive flow around an infinite cylinder with a transpiration (non-zero normal outward flow) boundary condition. The main finding is a direct correlation between the transpiration strength and the thickness of the thermal and solute boundary layers at the cylinder wall.

In the present work, we have used the non-trivial geometry consisting of two intersecting pipes shown in Figure 11. The mesh shown contains 25,696 linear tetrahedral elements and was carefully constructed using the Cubit (http://cubit.sandia.gov/) automatic mesh generator, with special care taken to ensure gradual element size transitions and element grading around the important geometric features, which in this case are the intersecting pipes. In the present application, the adaptive mesh refinement process does not interface with a geometry model, and therefore new nodes which are added as part of the adaptation process are *not* “snapped” to the original geometry. The initial coarse grid must therefore capture the essential features of the geometry while at the same time being coarse enough to allow for efficient adaptive simulations, since they cannot in principle coarsen below the level of the initial grid.

Motivated by the double-diffusive pipe flow configurations of Hasan and others, we set up the present problem so that the offset pipe (the pipe intersecting the front and back faces of the domain, not the corners) is held at fixed temperature and solute concentrations of $T = S = 1$. The solute concentration at the bottom of the domain (the pipes are cut from a unit cube centered at the origin, gravity is oriented in the $-y$

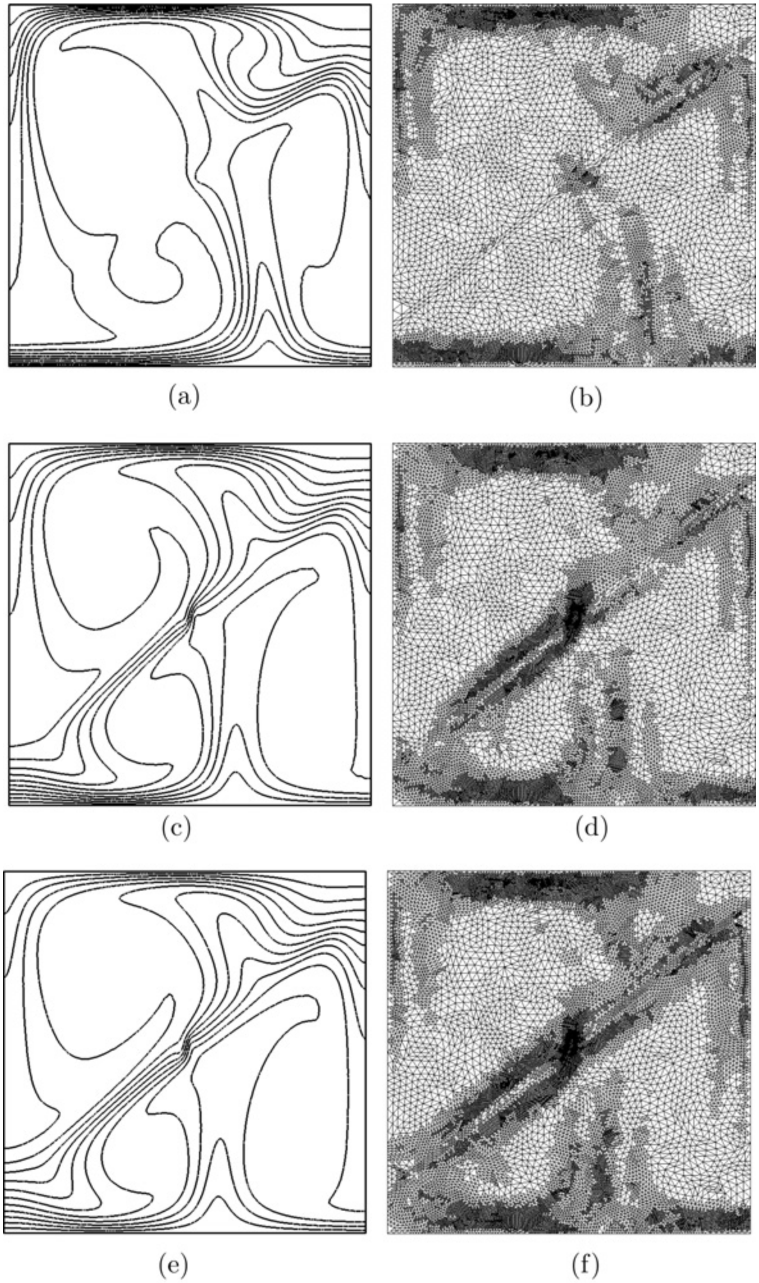

(a) (b) (c) (d) (e) (f)

Notes: (a) Solute contours, $K_b/K = 10^{-2}$, (b) mech: 20,474 cells, (c) solute contours, $K_b/K = 10^{-3}$, (d) mesh: 25,706 cells, (e) solute contours, $K_b/K = 10^{-4}$ and (f) mesh: 31,553 cells

Figure 10.
Steady solute contours and adapted grids for the semi-permeable barrier (as described in the text) for various permeability ratios

direction) is held fixed at $S = 0$, while the temperature at the top plane of the domain is held fixed at $T = 0$. The remaining faces of the cube and the diagonal pipe are all treated as insulated ($\partial T/\partial n = \partial S/\partial n = 0$) walls.

The value of κ was taken to be 0.1, and the thermal and solutal Rayleigh numbers in this case were $R_T = 20$ and $R_S = 16$, respectively, reduced from the typical 2D values of 200 and 160 since this 3D configuration is naturally unstable. (Recall that, in the 2D configuration, we were examining the onset of instability in a particular parameter regime.) Reducing the Rayleigh numbers reduces the convective velocities and makes the dynamics of the problem slower, but the boundary and internal layers can still be made arbitrarily thin by reducing κ.

A representative solution showing the evolving solute field in the angled pipe geometry is given in Figure 12(a). The mesh for this particular case is shown in Figure 12(b) and is a twice uniformly-refined version of the 25,696 element mesh shown in Figure 11. In this particular timestep, we observe a rising solute plume coming off the offset, heated pipe. Although the heavier fluid near the offset pipe naturally wants to fall (due to gravity) thermal buoyant forces propel it upward. The solute boundary layer near the bottom of the pipe is slightly thinner and is influenced by the nearby essential solute boundary condition imposed on the bottom of the domain.

The steady-state solute and temperature field configurations for this case are shown in Figures 12(c) and (d), respectively. At steady state the temperature and solute fields are once again quite different in character. The top of the domain is filled with fluid having a uniformly high solute concentration. This heavier fluid is suspended over a layer of lighter fluid which matches the essential $S = 0$ condition at the bottom of the wall. This inverted solute layer is disrupted by the presence of the pipe: we observe that the solute layer is drawn up slightly on either side, due to the existence of an upwelling caused by thermal buoyant effects near the hot pipe. The temperature boundary layer (at the top of the domain) is much less pronounced than the solute layer due to the mismatch in diffusivities present ($\kappa = 0.1$).

For moderate values of κ (such as the $\kappa = 0.1$ case on the uniform grid shown here) sharp boundary layers in the solute field do not dominate the solution. This situation changes as we begin to reduce κ, and in these cases mesh adaptivity is crucial for accurately capturing the solution. In Figure 13, we compare two representative cases where $\kappa = 0.0078$, both before and after multiple adaptive refinement steps. The before and after grids are shown in Figures 13(a) and (b), respectively. In these figures, the colors represent the domain decomposition onto four processors. The meshes are

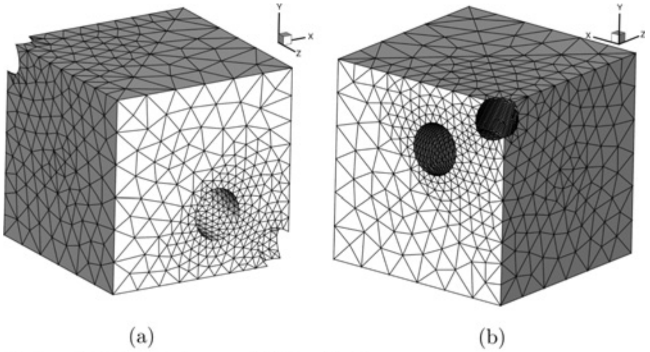

(a) (b)

Notes: (a) Front view and (b) back view

Figure 11.
Front and back views of the intersecting pipe mesh. The mesh has and 25,696 linear tetrahedral elements

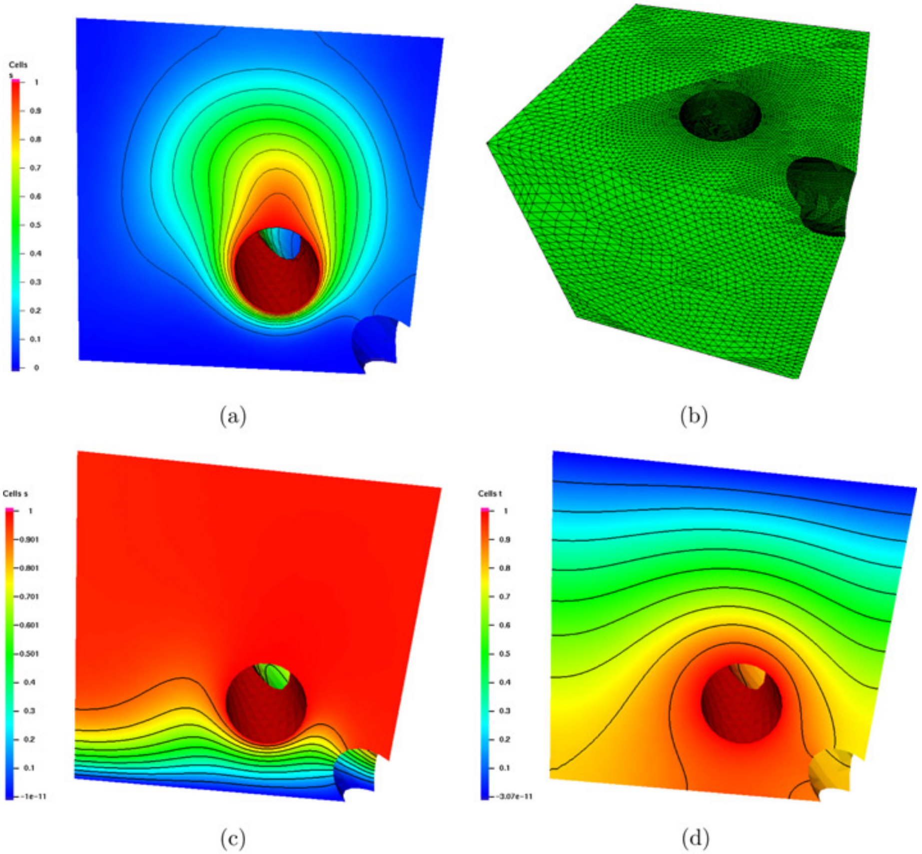

(a) (b)

(c) (d)

Figure 12.
Representative evolving solute field (Figure 12(a)) on a mesh (Figure 12(b)) with 1,644,544 elements, which is a twice-uniformly-refined version of the mesh shown in Figure 11. The steady-state solute (Figure 12(c)) and temperature (Figure 12(d)) configurations for the twice-uniformly-refined mesh with $\kappa = 0.1, R_T = 20$ and $R_S = 16$

Notes: (a) Evolving solute field, (b) uniformly refined mesh, (c) steady state solute field and (d) steady state temperature field

relatively coarse for this value of κ, and therefore the solution contours are not nearly as smooth as they were in the uniform grid case.

The solute fields before and after refinement are shown in Figures 13(c) and (d), respectively. We observe an improved capturing of the solute boundary layer near not only the bottom of the pipe, but also in the lower left-hand corner of the domain. The initial coarse grid is not well-designed to capture the solution features in this region (since the corner geometry is relatively simple) and does a poor job of resolving the layer. After several adaptive refinement steps, however, the boundary layer in this region is better resolved. An "entrainment" of low-solute fluid around the heated pipe rising from the bottom of the domain is again observed in this case, similar to what was seen previously, however, here the effect is much more pronounced and the entrainment extends further into the domain.

6. Concluding remarks

The non-linear behavior of double-diffusive convection in a heated, saturated porous medium is investigated. Of particular interest are: a horizontal layer heated from below

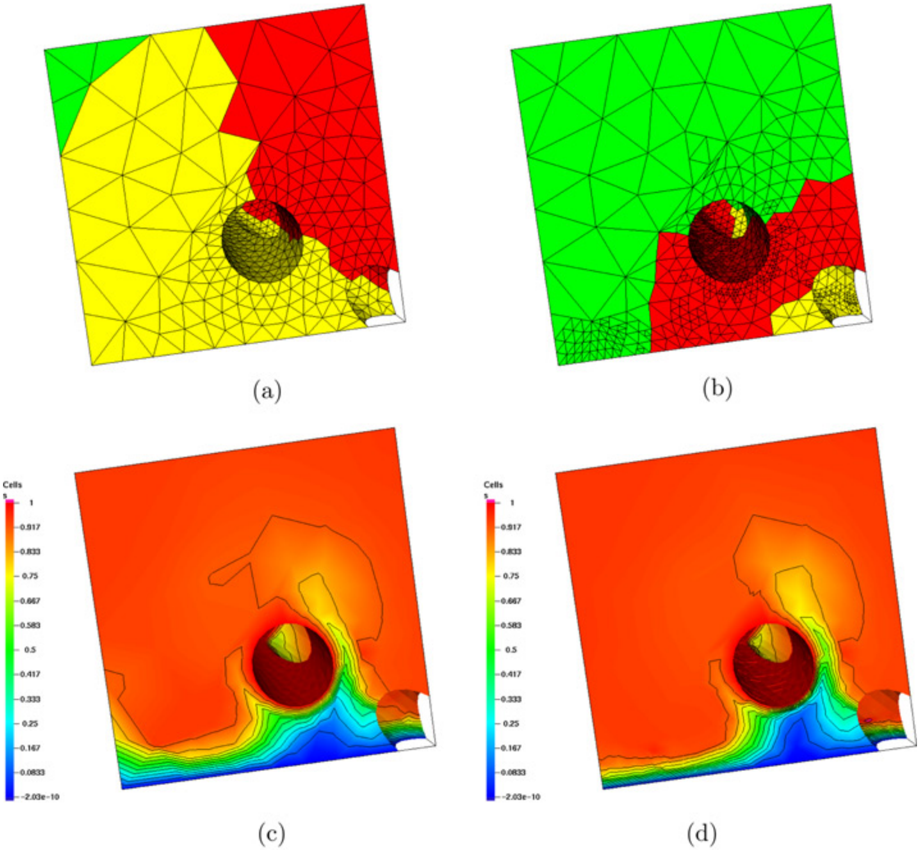

Notes: (a) Mesh, before refinement, (b) mesh, after refinement, (c) solute field, before refinement and (d) solute field, after refinement

Figure 13.
Comparison of the solute boundary layer solution before and after refinement, $\kappa = 0.0078$

with a stabilizing solute concentration gradient, problems with fine scale layers due to permeability streaks or local source effects, and similar issues related to the coupled multiphysics, multiscale character of the problem class. We have focused on Rayleigh number values largely in the regime of steady onset, even though this configuration may exhibit oscillatory onset based on linear stability theory. One example of the complex oscillatory behavior that occurs in finite amplitude solutions in the horizontal layer configuration was presented.

Small diffusivity ratio, κ, yields strong gradients in the solute concentration at the boundaries which must be properly resolved. Adaptive and uniform finite element solutions have been computed for varying values of the Lewis number, in two and three dimensions, using the "cold" wall Nusselt numbers to characterize the solutions. The results from analytical asymptotic theory for enclosed porous media boundary layers which predict square-root growth dependence of the Sherwood Number (solutal Nusselt number) in the chosen parameter regime were verified for the two-dimensional configurations tested. An analogous 3D study in a simple cube geometry was also undertaken and yielded axial sectional simulation plots (not shown here) that were similar to those of the 2D case. This led us to explore a 3D case with a more complex geometry composed of interior intersecting heated pipes in some detail. The parallel adaptive mesh refinement and coarsening capabilities of the `LibMesh` (Kirk *et al.*, 2006) library were demonstrated to be well-suited to the task of resolving fine scale behavior in the solute field below the heated pipe. The application code discussed here will also take advantage of the recently developed parallel mesh data structures present in `LibMesh`, allowing the simulations to scale well on modern hybrid multi-socket, multi-core computing platforms.

Using the statistical refinement and coarsening scheme with the local flux-jump error indicator it was found that, especially at large Lewis numbers, adaptive grids could achieve Sherwood number calculations with accuracy comparable to uniform grids having nearly five times more degrees of freedom. The increased cost for this accuracy (a single solution projection step followed by an additional nonlinear equation solve) is more than offset by the increased accuracy it affords. The adaptive scheme (with the particularly simple flux-jump error indicator chosen) is clearly the more efficient scheme for this quantity of interest, and in fact the scheme becomes even more efficient at higher Lewis numbers since the adaptivity becomes increasingly focused in thinner and thinner layers.

Another interesting aspect that bears further investigation is the concentrated heat and mass source problem (Poulikakos, 1985; Ganapathy, 1994; Hill, 2005) which has application to chemical and nuclear waste disposal problems. Very recently, the problem of reaction-driven, double-diffusive convection resulting from a stratified chemical front has been studied in some detail (Hernoncourt *et al.*, 2006). These broader applications of double-diffusive effects would appear to be well-suited to the adaptive methodology developed here.

Finally, fully three-dimensional, double-diffusive adaptive finite element studies for problems where the porosity is variable and may approach 1 in significant portions of the domain are of interest. In this case, Darcy's law alone may no longer be the appropriate model. The Brinkman model, where the Darcy viscous term is included in the Navier-Stokes equations, also has a wide range of applicability. This is an important area of further research which can be explored within the computational framework described here.

References

Aftosmis, M.J. and Berger, M.J. (2002), "Multilevel error estimation and adaptive *h*-refinement for Cartesian meshes with embedded boundaries", AIAA paper 2002-0863.

Ainsworth, M. and Oden, J.T. (2000), *A Posteriori Error Analysis in Finite Element Analysis*, Wiley Interscience, New York, NY.

Anderson, M.L., Bangerth, W. and Carey, G.F. (2005), "Analysis of parameter sensitivity and experimental design for a class of nonlinear partial differential equations", *International Journal of Numerical Methods in Fluids*, Vol. 48, pp. 583-605.

Angirasa, D. and Peterson, G.P. (1997), "Combined heat and mass transfer by natural convection with opposing buoyancy effects in a fluid saturated porous medium", *International Journal of Heat and Mass Transfer*, Vol. 40 No. 12, pp. 2755-73.

Babuška, I. and Rheinboldt, W.C. (1978), "A posteriori error estimates for the finite element method", *International Journal of Numerical Methods in Engineering*, Vol. 12, pp. 1597-615.

Balay, S., Eijkhout, V., Gropp, W.D., McInnes, L.C. and Smith, B.F. (1997), "Efficient management of parallelism in object oriented numerical software libraries", in Arge, E., Bruaset, A.M.

and Langtangen, H.P. (Eds), *Modern Software Tools in Scientific Computing*, Birkhäuser Press, pp. 163-202.

Bangerth, W. (2000), "Using modern features of C++ adaptive finite element methods: dimension-independent programming in deal.II", in Deville, M. and Owens, R. (Eds), *Proceedings of the 16th IMACS World Congress 2000, Lausanne*, Document Sessions/118-1.

Bangerth, W. and Kayser-Herold, O. (2008), "Data structures and requirements for *hp* finite element software", accepted for publication in ACM Transactions of Mathematical Software (this paper is also available as Technical Report ISC-07-04-MATH, Institute for Scientific Computation, Texas A&M University).

Bangerth, W. and Rannacher, R. (2003), *Adaptive Finite Element Methods for Differential Equations*, Birkhäuser Verlag, Berlin.

Bastian, P. *et al.* (1997), "UG – A flexible software toolbox for solving partial differential equations", *Computing and Visualization in Science*, Vol. 1, pp. 27-40.

Becker, E.B., Carey, G.F. and Oden, J.T. (1981), *Finite Elements – An Introduction*, Vol. 1, Prentice-Hall, Englewood Cliffs, NJ.

Bejan, A. (1984), *Convection Heat Transfer*, Wiley, New York, NY.

Bejan, A. and Khair, K.R. (1985), "Heat and mass transfer by natural convection in a porous medium", *International Journal for Heat and Mass Transfer*, Vol. 28, pp. 909-18.

Bennacer, R., Mahidjiba, A., Vasseur, P., Beji, H. and Duval, R. (2003), "The Soret effect on convection in a horizontal porous domain under cross temperature and concentration gradients", *International Journal of Numerical Methods for Heat and Fluid Flow*, Vol. 13, No. 2, pp. 199-215.

Brooks, A.N. and Hughes, T.J.R. (1982), "Streamline upwind/Petrov-Galerkin formulations for convection dominated flows with particular emphasis on the incompressible Navier-Stokes equations", *Computer Methods in Applied Mechanical and Engineering*, Vol. 32, pp. 199-259.

Budge, K. and Peery, J. (1996), "Experiences Developing ALEGRA: A C++ coupled physics Framework", in Henderson, M.E. Anderson, C.R. and Lyons, S.L. (Eds), *Object Oriented Methods for Interoperable Scientific and Engineering Computing*, Society for Industrial and Applied Mathematics, Philadelphia, PA.

Carey, G.F. (1997), *Computational Grids: Generation, Adaptation and Solution Strategies*, Taylor & Francis, London.

Carey, G.F., Barth, W., Woods, J.A., Kirk, B., Anderson, M.L., Chow, S. and Bangerth, W. (2004), "Modeling error and constitutive relations in simulation of flow and transport", *International Journal of Numerical Methods in Fluids*, Vol. 46, pp. 1211-36.

Carey, G.F., Chow, S. and Seager, M.R. (1985), "Approximate boundary-flux calculations", *CMAME*, Vol. 50, pp. 107-120.

Carey, G.F. and Humphrey, D.L. (1981), "Mesh refinement and iterative solution methods for finite element computations", *International Journal of Numerical Methods in Engineering*, Vol. 17, pp. 1717-34.

Carey, V., Estep, D. and Tavener, S. (2009), "A posteriori analysis and adaptive error control for operator decomposition solution of elliptic systems I: triangular systems", *SIAM J. Numerical Analysis*, Vol. 47 No. 1, pp. 740-61.

Cheng, P. (1978), "Heat transfer in geothermal systems", *Advanced Heat Transfer*, Vol. 14, pp. 1-105.

Cross, J.T., Masters, I. and Lewis, R.W. (1999), "Why you should consider object-oriented programming techniques for finite element methods", *International Journal of Numerical Methods for Heat and Fluid Flow*, Vol. 9 No. 3, pp. 333-47.

D'Hernoncourt, J., Zebib, A. and Wit, A.D. (2006), "Reaction driven convection around a stably stratified front", *Physical Review Letters*, Vol. 96 No. 15, Art. No. 154104.

Debeda, V., Caltagirone, J.P. and Watremez, P. (1995), "Local multigrid refinement method for natural convection in fissured porous media", *Numerical Heat Transfer B*, Vol. 28, pp. 455-67.

Devloo, P.R.B. and Longhin, G.C. (2002), "Object oriented design philosophy for scientific computing", *Mathematical Modelling and Numerical Analysis*, Vol. 36, pp. 793-807.

Diersch, H.-J.G. and Kolditz, O. (2002), "Variable-density flow and transport in porous media: approaches and challenges", *Advanced Water Resources*, Vol. 25, pp. 899-944.

Estep, D., Carey, V., Ginting, V., Tavener, S. and Wildey, T. (2008), "A posteriori error analysis of multiscale operator decomposition methods for multiphysics models", *Journal of Physics: Conference Series*, Vol. 125, pp. 1-16.

Felicelli, S.D., Heinrich, J.C. and Poirier, D.R. (1998), "Finite element analysis of directional solidification of multicomponent alloys", *International Journal of Numerrical Methods in Fluids*, Vol. 27, pp. 207-27.

Gallagher, R.H., Oden, J.T., Zienkiewicz, O.C., Kawai, T. and Kawahara, M. (Eds) (1984), *Finite Elements in Fluids*, Vol. 5, Wiley, New York, NY.

Ganapathy, R. (1994), "Free convection flow induced by a line source in a sparsely packed porous medium", *Advanced Water Resources*, Vol. 17, pp. 251-58.

Gartling, D.K. (1982), "Finite element analysis of thermal convection in deep ocean sediments", *Advanced Water Resources*, Vol. 5, pp. 136-41.

Gobin, D. and Goyeau, B. (2008), "Natural convection in partially porous media: a brief overview", *International Journal of Numerical Methods for Heat and Fluid Flow*, Vol. 18 Nos. 3/4, pp. 465-90.

Gray, W.G. (1975), "A derivation of the equations for multiphase transport", *Chemical Engineering Science*, Vol. 30, pp. 229-33.

Gresho, P.M. and Sani, R.L. (1998), *Incompressible Flow and the Finite Element Method*, Wiley, New York, NY.

Hasan, M. and Mujumdar, A.S. (1985), "Transpiration-induced buoyancy effect around a horizontal cylinder embedded in a porous medium", *Energy Research*, Vol. 9, pp. 151-63.

Heinrich, J.C. and Pepper D.W. (1999), *Intermediate Finite Element Method: Fluid Flow And Heat Transfer Applications*, Taylor & Francis, London.

Heinrich, J.C. and Poirier, D.R. (2004), "Convection modeling in directional solidification", *Comptes Rendus Mécanique*, Vol. 332, pp. 429-45.

Hickox, C.E., Gartling, D.K., McVey, D.F. and Russo, A.J. (1982), "Analysis of heat and mass transfer in subseabed disposal of nuclear waste", *Marine Geotechnology*, Vol. 5 Nos. 3/4, pp. 335-60.

Hill, A.A. (2005), "Double-diffusive convection in a porous medium with a concentration based internal heat source", *Proceedings of the Royal Society A*, Vol. 461, pp. 561-74.

Hughes, T.J.R. (1987), *Finite Element Method – Linear Static and Dynamic Finite Element Analysis*, Prentice-Hall, Englewood Cliffs, NJ.

Jellinek, A.M. and Kerr, R.C. (1999), "Mixing and compositional stratification produced by natural convection. Part 2: applications to the differentiation of basaltic and silicic magma chambers and komatiite lava flows", *Journal of Geophysics Resources*, Vol. 104, pp. 7203-219.

Jellinek, A.M., Kerr, R.C. and Griffiths, R.W. (1999), "Mixing and compositional stratification produced by natural convection. Part 1. The experiments and their application to Earth's core and mantle", *Journal of Geophysics Resources*, Vol. 104, pp. 7183-202.

Johnson, C. (1987), *Numerical Solution of Partial Differential Equations by the Finite Element Method*, Cambridge University Press, Cambridge.

Karypis, G. and Kumar, V. (1998), "A parallel algorithm for multilevel graph partitioning and sparse matrix reordering", *Parallel and Distributed Computing*, Vol. 48, pp. 71-95.

Kelly, D.W., Gago, J.P., Zienkiewicz, O.C. and Babuska, I. (1983), "A posteriori error analysis and adaptive processes in the finite element method: part I error analysis", *International Journal of Numerical Methods in Engineering*, Vol. 19, pp. 1593-619.

Kirk, B., Peterson, J.W., Stogner, R.H. and Carey, G.F. (2006), "`LibMesh`: a C++ library for parallel adaptive mesh refinement/coarsening simulations", *Engineering with Computers*, Vol. 22 Nos. 3/4, pp. 237-54, available at: http://dx.doi.org/10.1007/s00366-006-0049-3

Lewis, R.W., Nithiarasu, P. and Seetharamu, K. (2004), *Fundamentals of the Finite Element Method for Heat and Fluid Flow*, Wiley, New York, NY.

Luo, Y.Y., Zhan, J.M. and Li, Y.S. (2008), "Numerical simulation of salt finger convection in porous media", *Acta Physica Sinica*, Vol. 57, pp. 2306-13.

McKibbin, R. (1986), "Heat transfer in a vertically-layered porous medium heated from below", *Transport in Porous Media*, Vol. 1, pp. 361-70.

McKibbin, R. and Tyvand, P.A. (1984), "Thermal convection in a porous medium with horizontal cracks", *International Journal of Heat and Mass Transfer*, Vol. 27, pp. 1007-23.

Mamou, M. and Vasseur, P. (1999), "Thermosolutal bifurcation phenomena in porous enclosures subject to vertical temperature and concentration gradients", *Journal of Fluid Mechanical*, Vol. 395, pp. 61-87.

Nguyen-Quang, T., Nguyen, H. and Lepalec, G. (2008), "Gravitactic bioconvection in a fluid-saturated porous medium with double diffusion", *Journal of Porous Media*, Vol. 11, pp. 751-64.

Nield, D.A. (1968), "Onset of thermohaline convection in a porous medium", *Water Resources Res.*, Vol. 4, pp. 553-60.

Nield, D.A. and Bejan, A. (1999), *Convection in Porous Media*, Springer, Berlin.

Pehlivanov, A., Lazarov, R., Carey, G.F. and Chow, S. (1992), "Superconvergence analysis of approximate boundary-flux calculations", *Numerische Mathematik*, Vol. 63, pp. 483-501.

Peterson, J.W., Carey, G.F., Knezevic, D.J. and Murray, B.T. (2007), "Adaptive finite element methodology for tumor angiogenesis modeling", *International Journal of Numerical Methods Engineering*, Vol. 69 No. 6, pp. 1212-38, available at: http://dx.doi.org/10.1002/nme.1802

Poulikakos, D. (1985), "On buoyancy-induced heat and mass transfer from a concentrated source in an infinite porous medium", *International Journal of Heat and Mass Transfer*, Vol. 28, pp. 621-29.

Rebaï, L.K., Mojtabi, A., Safi, M.J. and Mohamad, A.A. (2008), "Numerical study of thermosolutal convection with Soret effect in a square cavity", *International Journal of Numerical Methods for Heat and Fluid Flow*, Vol. 18 No. 5, pp. 561-74.

Rudraiah, N., Siddheshwar, P.G. and Masuoka, T. (2003), "Nonlinear convection in porous media: a review", *Journal of Porous Media*, Vol. 6, pp. 1-32.

Sezai, I. (2002), "Flow transitions in three-dimensional double-diffusive fingering convection in a porous cavity", *Journal of Fluid Mechanical*, Vol. 464, pp. 311-44.

Shakib, F., Hughes, T.J.R. and Johan, Z. (1991), "A new finite element formulation for computational fluid dynamics: X. The compressible Euler and Navier-Stokes equations", *Computer Methods in Applied Mechanics and Engineering*, Vol. 89, pp. 141-219.

Smith, G.D. (1996), *Numerical Solution of Partial Differential Equations*, 3rd ed., Oxford University Press, New York, NY.

Solin, P. and Demkowicz, L. (2004), "Goal-oriented *hp*-adaptivity for elliptic problems", *Computer Methods in Applied Mechanical and Engineering*, Vol. 193, pp. 449-68.

Strang, G. and Fix, G.J. (1973), *An Analysis of the Finite Element Method*, Prentice-Hall, Englewood Cliffs, NJ.

Trevisan, O.V. and Bejan, A. (1985), "Natural convection with combined heat and mass transfer buoyancy effects in a porous medium", *International Journal of Heat and Mass Transfer*, Vol. 28, pp. 1597-611.

Trevisan, O.V. and Bejan, A. (1986), "Mass and heat transfer by natural convection in a vertical slot filled with porous medium", *International Journal of Heat and Mass Transfer*, Vol. 29, pp. 403-15.

Wooding, R.A. (1959), "The stability of a vertical tube containing porous material", *Proceeding of the Royal Society of London A*, Vol. 252, pp. 120-34.

Zabaras, N. and Samanta, D. (2004), "A stabilized volume-averaging finite element method for flow in porous media and binary alloy systems", *International Journal of Numerical Methods in Engineering*, Vol. 60, pp. 1103-38.

Zhan, J.M. and Li, Y.S. (2003), "Numerical simulation of unsteady flow in natural and thermosolutal convection using boundary-fitted coordinate system", *International Journal of Numerical Methods for Heat and Fluid Flow*, Vol. 13 No. 8, pp. 1031-56.

Zienkiewicz, O.C. and Zhu, J.Z. (1987), "A simple error estimator and adaptive procedure for practical engineering analysis", *International Journal of Numerical Methods Engineering*, Vol. 24, pp. 337-57.

Zienkiewicz, O.C. and Zhu, J.Z. (1992), "The superconvergent patch recovery and a-posteriori error estimates. part I: the recovery technique", *International Journal of Numerical Methods Engineering*, Vol. 33, pp. 1331-64.

Appendix. Visualization

For purposes of flow visualization, it is convenient to plot the components of the Darcy velocity $\boldsymbol{u}^h$ as a continuous vector field. Unfortunately,

$$\boldsymbol{u}^h = \hat{\boldsymbol{K}}(\boldsymbol{b}^h - \nabla p^h)$$

is a piecewise-discontinuous function when a standard C^0 continuous Lagrange basis is used to compute p^h, T^h, and S^h. One method for obtaining the continuous vector field plots is to solve a global constrained L_2-projection problem for the velocity. We recognize that there are local, easily parallelizable schemes for obtaining the continuous velocity (e.g. the patch recovery method (Zienkiewicz and Zhu, 1992)). However, since the present L_2-projection process is inexpensive and only required here for visualization purposes, the computational efficiency of the scheme is not of primary importance.

The constrained L_2-projection problem is obtained by seeking the continuous vector function $\boldsymbol{u}_c$ which minimizes

$$F(\boldsymbol{u}_c) = \frac{1}{2}\int_\Omega |\boldsymbol{u}_c - \boldsymbol{u}^h|^2\,dx + \frac{1}{2\epsilon}\int_{\partial\Omega} (\boldsymbol{u}_c \cdot \hat{n} - g_N)^2\,ds \tag{A1}$$

In the surface integral of equation (A.1), g_N is the prescribed value of $\boldsymbol{u} \cdot \hat{\boldsymbol{n}}$ on the boundary. For $\epsilon \ll 1$, this term effectively constrains the recovered velocity field $\boldsymbol{u}_c$ to match the in/outflow conditions set for the original problem. Setting the first variation $\delta F(\boldsymbol{u}_c) = 0$ then yields

$$\int_\Omega (\boldsymbol{u}_c - \boldsymbol{u}^h) \cdot \delta\boldsymbol{u}_c\,dx + \frac{1}{\epsilon}\int_{\partial\Omega} (\boldsymbol{u}_c \cdot \hat{n} - g_N)(\delta\boldsymbol{u}_c \cdot \hat{n})\,ds = 0 \tag{A2}$$

Interpreting the variational quantity $\delta\boldsymbol{u}_c$ as a test function $\boldsymbol{v}$ from a particular space of test functions $\mathcal{V}$, we then seek $\boldsymbol{u}_c \in \mathcal{V}$ such that

$$\int_{\Omega} \boldsymbol{u}_c \cdot \boldsymbol{v}\, dx + \frac{1}{\epsilon}\int_{\partial\Omega} (\boldsymbol{u}_c \cdot \hat{n})(\boldsymbol{v} \cdot \hat{n})\, ds = \int_{\Omega} \boldsymbol{u}^h \cdot \boldsymbol{v}\, dx + \frac{1}{\epsilon}\int_{\partial\Omega} g_N(\boldsymbol{v} \cdot \hat{n})\, ds \qquad \text{(A3)}$$

for every $\boldsymbol{v} \in \mathcal{V}$. Choosing an approximation space $\mathcal{V}^h \subset \mathcal{V}$ (for example the same C^0 continuous Lagrange basis used in the original problem) leads to a well-posed, symmetric system of linear equations for the post-processed velocity $\boldsymbol{u}_c^h$. In the results sections of the paper, whenever velocity vectors are shown, they will be assumed to be from the continuous recovered velocity field $\boldsymbol{u}_c^h$.

About the authors

J.W. Peterson received his Bachelor of Science (with honors) degree in Aerospace Engineering, Master of Science in Engineering in May 2003 under advisor, and PhD from the University of Texas at Austin. During his graduate career, John was both a NASA Graduate Student Research Fellow and a University of Texas Thrust 2000 Graduate Fellow. He has served as a teaching assistant, guest lecturer, and full lecturer during his graduate career. Other activities have included management and systems administration for a Linux computer lab and peer reviewing for several numerical engineering journals. He is currently a Research Associate at the Texas Advanced Computing Center, where he is a member of the HPC applications group. J.W. Peterson is the corresponding author and can be contacted at: peterson@tacc.utexas.edu

B.T. Murray was formerly at the National Institute of Standards and Technology in Gaithersburg, Maryland where he worked in the area of computational materials science. He has also held a faculty position in the Department of Mechanical Engineering and Mechanics at Lehigh University and was a Member of Technical Staff at Bell Laboratories (now Lucent Technologies). His research interests are in the areas of materials processing, convective heat and mass transfer, and computational methods. He is associated with the Physicochemical Hydrodynamics Laboratory and the Materials Laboratory in the ME Department. Two recent collaborative projects concern transport effects in crystal growth and computational modeling of dendritic solidification.

G.F. Carey is a member of the interdisciplinary Institute for Computational Engineering and Sciences (ICES) and a Professor in the Department of Aerospace Engineering and Engineering Mechanics at the University of Texas at Austin and holder of the Richard B. Curran Centennial Chair in Engineering. He is Director of the Computational Fluid Dynamics Laboratory. He has a BS (Hons.) degree from Australia, and MS and PhD degrees from the University of Washington at Seattle. His research and teaching activities primarily deal with techniques in computational mechanics, particularly finite element methods and supercomputing. Related research experience includes periods as a research faculty member in Civil Engineering Australia (1966-1968), and as a research engineer at the Boeing Company, Seattle (1968-1970), during which time he worked in finite element formulation and computation of nonlinear problems. Prior to joining the University of Texas faculty, he held the positions of Research Assistant to Research Associate Professor at the University of Washington (1974-1976), working on computational problems in mechanics.